5074 *Chem. Mater.* **2010,** *22,* 5074–5083
DOI:10.1021/cm1011839

CHEMISTRY OF MATERIALS
Article

Experimental and Computational Investigation of the Polar Ferrimagnet $VOSe_2O_5$

Sang-Hwan Kim,[†] P. Shiv Halasyamani,*[,†] Brent C. Melot,[‡] Ram Seshadri,[‡] Mark A. Green,[§] Athena S. Sefat,[∥] and David Mandrus[∥,⊥]

[†]*Department of Chemistry, University of Houston, 136 Fleming Building, Houston, Texas 77204-5003,* [‡]*Materials Department and Materials Research Laboratory, University of California, Santa Barbara, California 93106-5121,* [§]*Department of Materials Science and Engineering, University of Maryland, College Park, Maryland 20742-2115 and NIST Center for Neutron Research, National Institute of Standards and Technology, 100 Bureau Drive, Gaithersburg, Maryland 20899-6103,* [∥]*Materials Science and Technology Division, Oak Ridge National Laboratory, Oak Ridge, Tennessee 37831, and* [⊥]*Department of Materials Science and Engineering, 325 Dougherty Hall, The University of Tennessee and Oak Ridge National Laboratory, Knoxville, Tennessee 37996*

Received April 27, 2010. Revised Manuscript Received June 8, 2010

We have re-examined the crystal structure and the physical properties of $VOSe_2O_5$ by performing single crystal X-ray and powder neutron diffraction, alternating current (AC) and direct current (DC) magnetization measurements, heat capacity, dielectric properties, and second-harmonic generation (SHG) measurements. From these studies, we observed that the compound undergoes three *magnetic* transitions near 4, 5.5, and 8 K. In addition, we observed ferrimagnetic behavior as the magnetic ground state, confirmed by the isothermal magnetization measured below 8 K that reveals a saturated magnetic moment of 0.5 μ_B per formula unit, consistent with density functional calculations of the magnetically ordered ground state. We propose a ferrimagnetic spin arrangement that is consistent with neutron diffraction measurements as well. Frequency dependence in the AC magnetic susceptibility, observed at 5.5 K, is considered as short-range magnetic ordering and may be associated with the competition between nearest neighbor and next nearest neighbor interactions of the V^{4+} cations. A dielectric anomaly near 240 K and non-centrosymmetric functional properties, notably, second harmonic generation and electric polarization, are also discussed.

Introduction

Multifunctional oxide materials are of great current interest as a consequence of their many possible applications in next generation technologies. In particular, magnetoelectric multiferroics,[1−6] materials in which an electric polarization coexists with a magnetically ordered phase, are potentially useful for new sensors, and for data storage, and suggest novel approaches to computation. Such multiferroics are rare, since magnetic ordering and ferroelectricity generally require contradictory valence-shell configurations[7]: magnetic ordering requires the presence of unpaired electrons in the valence shell, whereas ferroelectric materials generally have empty valence shells that can hybridize with surrounding anions.[8−13] In addition, ferroelectricity requires macroscopic electric polarization that must be "switchable" in the presence of an external electric field. The macroscopic polarization implies that any inversion center in the crystal structure is broken through either a structural distortion and/or magnetic ordering.[3,14−16]

Given the contraindicated nature of the multiferroics, a useful starting point to discover new multiferroics would be to examine polar non-centrosymmetric materials that contain magnetic cations. Materials of this type include $BiFeO_3$[14] and $MnWO_4$,[17,18] as well as $BaNiF_4$.[19] With respect to polar non-centrosymmetric V^{4+} oxides, $PbVO_3$ has been reported and recently grown as thin films.[20,21]

*To whom correspondence should be addressed. E-mail: psh@uh.edu.

(1) Eerenstein, W.; Mathur, N. D.; Scott, J. F. *Nature* **2006**, *442*, 759.
(2) Fiebig, M. *J. Phys. D: Appl. Phys.* **2005**, *38*, R123.
(3) Hur, N.; Park, S.; Sharma, P. A.; Ahn, J. S.; Guha, S.; Cheong, S. W. *Nature* **2004**, *429*, 392.
(4) Kimura, T.; Goto, T.; Shintani, H.; Ishizaka, K.; Arima, T.; Tokura, Y. *Nature* **2003**, *426*, 55.
(5) Scott, J. F. *Nat. Mater.* **2007**, *6*, 256.
(6) Spaldin, N. A.; Fiebig, M. *Science* **2005**, *309*, 391.
(7) Hill, N. A. *J. Phys. Chem. B* **2000**, *104*, 6694.
(8) Bader, R. F. W. *Mol. Phys.* **1960**, *3*, 137.
(9) Bader, R. F. W. *Can. J. Chem.* **1962**, *40*, 1164.
(10) Goodenough, J. B. *Annu. Rev. Mater. Sci.* **1998**, *28*, 1.
(11) Pearson, R. G. *J. Am. Chem. Soc.* **1969**, *91*, 4947.
(12) Pearson, R. G. *J. Mol. Struct.:THEOCHEM* **1983**, *103*, 25.
(13) Wheeler, R. A.; Whangbo, M. H.; Hughbanks, T.; Hoffmann, R.; Burdett, J. K.; Albright, T. A. *J. Am. Chem. Soc.* **1986**, *108*, 2222.
(14) Fischer, P.; Polomska, M.; Sosnowska, I.; Szymanski, M. *J. Phys. C* **1980**, *13*, 1931.
(15) Singh, D. J. *Phys. Rev. B* **2006**, *73*, 094102-1.
(16) Goto, T.; Kimura, T.; Lawes, G.; Ramirez, A. P.; Tokura, Y. *Phys. Rev. Lett.* **2004**, *92*, 257201.
(17) Taniguchi, K.; Abe, N.; Takenobu, T.; Iwasa, Y.; Arima, T. *Phys. Rev. Lett.* **2006**, *97*, 097203.
(18) Arkenbout, A. H.; Palstra, T. T. M.; Siegrist, T.; Kimura, T. *Phys. Rev. B* **2006**, *74*, 184431.
(19) Ederer, C.; Spaldin, N. A. *Phys. Rev. B* **2006**, *74*, 024102.
(20) Kumar, A.; Martin, L. W.; Denev, S.; Kortright, J. B.; Suzuki, Y.; Ramesh, R.; Gopalan, V. *Phys. Rev. B* **2007**, *75*, 060101–1.

 Published on Web 08/04/2010

This material contains a cation with a lone-pair, Pb^{2+}, and was recently shown to be antiferromagnetic with an ordering temperature between 43 and 50 K.[21] In this contribution, we investigate $VOSe_2O_5$, a magnetically ordered material that crystallizes in the polar non-centrosymmetric space group $P4cc$.[22,23] The structure consists of three independent chains of corner-shared VO_6 octahedra that run parallel to the c-axis. The VO_6 octahedral chains are connected by a Se_2O_5 group, parallel to the a- and b-axes. The Se_2O_5 group can be visualized as two corner sharing SeO_3 trigonal pyramids that each exhibits a stereochemically active lone-pair at the apex of the pyramids. The stereoactive lone-pairs are directed in an antiparallel manner. Previous work had noted complicated magnetic behavior below 10 K, and ferromagnetic ordering near 4 K.[22] This was, however, based solely upon temperature-dependent susceptibility data. No additional investigation has been performed to further characterize the magnetic, dielectric, and functional properties of this potentially very interesting material.

We have used magnetic susceptibility, heat capacity, dielectric, second-harmonic generation, and powder neutron diffraction measurements, as well as density functional theory (DFT) calculations to elucidate the functional properties of $VOSe_2O_5$. Additionally, we have resolved and improved upon the crystal structure using single crystal X-ray diffraction. The dielectric properties show no evidence of an anomaly associated with the magnetic ordering. A peak is observed near 240 K that is, however, unaffected by the application of a magnetic field. Using neutron diffraction data in combination with DFT calculations, we propose a ferrimagnetic structure that is consistent with our theoretical and experimental results.

Experimental Details

Synthesis. $VOSe_2O_5$ was prepared via conventional solid state synthesis. Stoichiometric amounts of VO_2 and SeO_2 (99.8%, Alfa Aesar) were thoroughly ground, mixed, and pressed in a pellet. The pellet was placed in a pyrex tube that was flame-sealed under vacuum. The sealed ampule was heated at 400 °C for 4 days with several intermediate grindings giving a product consisting of pale green crystals. VO_2 was prepared from a stoichiometric mixture of V_2O_5 (99.9%, Alfa Aesar) and V_2O_3. The V_2O_3 was prepared by reduction of V_2O_5 under flowing 5%-H_2 in N_2 gas at 900 °C. Phase purity was confirmed using powder X-ray diffraction collected on a PANalytical X'Pert PRO diffractometer using Cu−Kα radiation.

Single Crystal X-ray Diffraction. A pale green rod-shaped crystal (ca. $0.20 \times 0.01 \times 0.01$ mm^3) was chosen for single crystal X-ray diffraction. The data were collected using a Siemens SMART APEX diffractometer equipped with a 1K CCD area detector using graphite-monochromated Mo-$K\alpha$ radiation. A hemisphere of data was collected using a narrow-frame method with scan widths of 0.30° in ω, and an exposure time of 30 s per frame. The data were integrated using the Siemens SAINT program,[24] with the intensities corrected for Lorentz-Polarization, air absorption, and absorption attributable to the variation in the path length through the detector face plate. ψ-scans were used for the absorption correction on the data.[24] The data were solved by direct methods and refined against F^2 by full-matrix least-squares techniques using SHELXS-97 and SHELXL-97, respectively.[25−27] All of the atoms in the structure were refined with anisotropic thermal parameters, and the refinements converged for $I > 2\sigma(I)$. The Flack parameter refined to −0.01(1). The structure was checked for missing symmetry elements using PLATON.[28] Relevant crystallographic data, atomic coordinates, and thermal parameters, and selected bond distances for $VOSe_2O_5$ are given in Tables 1, 2, and 3, respectively.

Table 1. Single Crystal Data of $VOSe_2O_5$ and Structure Refinement Parameters

space group, Z	$P4cc$ (no. 103), 8
formula weight	304.86
lattice parameters (Å)	a = 11.2338(8)
	c = 7.8711(11)
ρ_{calcd}(g/cm^3)	4.077
μ (Mo Kα, mm^{-1})	16.603
$R(F)^a$, $R_W(F^2)^b$	0.0206, 0.0288

^{a} $R = \sum||F_o| - |F_c||/\sum|F_o|$. ^{b} $R_W = \{\sum w(F_o^2 - F_c^2)^2/\sum w(F_o^2)^2\}^{1/2}$.

Table 2. Atomic Positions and Isotropic Equivalent Displacement Parameters ($\times 10^3$ Å^2) for $VOSe_2O_5$

	Wyck	x	y	z	U_{eq}[a]
V(1)	2a	0	0	0.91485(18)	8.6(3)
V(2)	2b	1/2	1/2	0.67084(17)	8.0(3)
V(3)	4c	0	1/2	0.74483(13)	9.99(17)
Se(1)	8d	0.21837(3)	0.86730(3)	0.73783(4)	10.40(8)
Se(2)	8d	0.25936(3)	0.60346(3)	0.84145(5)	10.89(8)
O(1)	2a	0	0	0.1202(7)	13.3(13)
O(2)	2b	1/2	1/2	0.4637(8)	13.4(13)
O(3)	4c	0	1/2	0.9475(4)	15.9(9)
O(4)	8d	0.3781(2)	0.6231(2)	0.7125(3)	14.0(6)
O(5)	8d	0.1725(2)	0.9752(2)	0.8739(3)	11.8(6)
O(6)	8d	0.3561(2)	0.9046(2)	0.6896(3)	18.7(7)
O(7)	8d	0.1485(2)	0.5935(2)	0.7007(3)	16.9(6)
O(8)	8d	0.2456(2)	0.7559(2)	0.9017(3)	14.4(6)

[a] U_{eq} is defined as a third of the trace of the orthogonalized $\mathbf{U}_{ij}$ tensor.

Powder X-ray Diffraction. Powder X-ray diffraction (PXRD) data were collected using a PANalytical X'Pert PRO diffractometer using Cu−Kα radiation. The 2θ range was 5°−100° with a step size of 0.0167° and a fixed time of 0.2s. The PXRD pattern is in good agreement with the calculated PXRD from the single crystal model (see Supporting Information, Figure S1).

Neutron Powder Diffraction. Constant wavelength neutron diffraction data were obtained at temperatures of 10 K, 8 K, 6 K, and 4 K. The data were collected using the BT-1 diffractometer at the NIST Center for Neutron Research (NCNR), over the range of 1.3°−166.3° 2θ with a step size of 0.05°. A Ge(311) monochromator at a 75° takeoff angle and 15′ in-pile collimator

(21) Shpanchenko, R. V.; Chernaya, V. V.; Tsirlin, A. A.; Chizhov, P. S.; Sklovsky, D. E.; Antipov, E. V.; Khlybov, E. P.; Pomjakushin, V.; Balagurov, A. M.; Medvedeva, J. E.; Kaul, E. E.; Geibel, C. *Chem. Mater.* **2004**, *16*, 3267.
(22) Trombe, J. C.; Gleizes, A.; Galy, J.; Renard, J. P.; Journaux, Y.; Verdaguer, M. *New J. Chem.* **1987**, *11*, 321.
(23) Meunier, G.; Bertaud, M.; Galy, J. *Acta Crystallogr., Sect. B* **1974**, *B30*, 2834.
(24) *SAINT, Program for Area Detector Absorption Correction*, 4.05; Siemens Analytical X-ray Systems, Inc.: Madison, WI, 1995.
(25) Sheldrick, G. M. *SHELXL-97 - A program for crystal structure refinement*; University of Goettingen: Goettingen, Germany, 1997.
(26) Sheldrick, G. M. *SHELXS-97 - A program for automatic solution of crystal structures*; University of Goettingen: Goettingen, Germany, 1997.
(27) Sheldrick, G. M. *SHELXTL DOS/Windows/NT*, 5.10; Bruker Analytical X-Ray Instruments, Inc.: Madison, WI, 1997.
(28) Spek, A. L. *PLATON*; Utrecht University: Utrecht, The Netherlands, 2001.

Table 3. Selected Bond Distances (Å) and Selected Bond Angles (deg) in $VOSe_2O_5$

V(1)−O(1)	1.616(6)	O(1)−V(1)−O(1)	180.000(3)
	2.319(6)	O(5)−V(1)−O(5)	161.32(16) × 2
V(1)−O(5)	1.984(2) × 4	O(2)−V(2)−O(2)	180.000(3)
V(2)−O(2)	1.630(6)	O(4)−V(2)−O(4)	160.85(16) × 2
	2.305(6)	O(3)−V(3)−O(3)	180.000(2)
V(2)−O(4)	1.973(2) × 4	O(6)−V(3)−O(6)	154.73(15)
V(3)−O(3)	1.595(3)	O(7)−V(3)−O(7)	160.00(15)
	2.341(3)		
V(3)−O(6)	1.988(3) × 2	O(5)−Se(1)−O(6)	104.39(12)
V(3)−O(7)	2.002(2) × 2	O(5)−Se(1)−O(8)	95.44(11)
		O(6)−Se(1)−O(8)	100.37(12)
Se(1)−O(5)	1.698(2)	O(4)−Se(2)−O(7)	101.47(13)
Se(1)−O(6)	1.647(3)	O(4)−Se(2)−O(8)	95.90(11)
Se(1)−O(8)	1.823(2)	O(7)−Se(2)−O(8)	100.14(12)
Se(2)−O(4)	1.691(3)		
Se(2)−O(7)	1.670(2)		
Se(2)−O(8)	1.783(2)		

were used, resulting in $\lambda = 2.0787(2)$ Å. The instrument is described at the NCNR Web site (http://www.ncnr.nist.gov/). Rietveld refinements of the structure against the diffraction data were performed by using the FULLPROF software package.[29] A group theoretical analysis, using representational analysis as implemented in the program SARA*h*,[30] was used to determine all of the possible spin configurations which were compatible with the crystal symmetry. Time-of-flight (TOF) neutron powder diffraction data on samples held in vanadium cans were also collected at the NPDF instrument at Los Alamos National Laboratory at several temperatures from room temperature to 6 K. Rietveld refinement of the structure against the TOF data were performed using GSAS suite of programs.[31,32]

Thermogravimetric Analysis. Thermogravimetric analysis was carried out on a TGA 951 thermogravimetric analyzer (TA Instruments). The sample was placed in a platinum crucible and heated at a rate of 10 °C min^{-1} from room temperature to 900 °C under flowing nitrogen. The TGA data has been deposited in the Supporting Information, Figure S2.

UV−vis Diffuse Reflectance Spectroscopy. UV−visible reflectance data were collected on a Varian Cary 500 scan UV−vis−NIR spectrophotometer over the 200−2000 nm spectral range at room temperature. Poly(tetrafluoroethylene) was used as a reference material. The reflectance spectrum was converted to absorbance using the Kubelka−Munk function (see the Supporting Information, Figure S3).[33,34]

Second Harmonic Generation. Powder SHG measurements were performed on a modified Kurtz-NLO[35] system using a pulsed Nd:YAG laser with a wavelength of 1064 nm. A detailed description of the equipment and methodology has been published.[36] The SHG efficiency has been shown to depend strongly upon particle size, thus polycrystalline samples were ground and sieved into distinct particle size ranges (20−45, 45−63, 63−75, 75−90, > 90 μm).[35] To make relevant comparisons with known SHG materials, crystalline α-SiO_2 and $LiNbO_3$ were also ground and sieved into the same particle size ranges (see Noncentrosymmetric Functional Properties section). No index matching fluid was used in any of the experiments.

Polarization Measurements. The polarization was measured on a Radiant Technologies RT66A Ferroelectric Test System with a TREK high voltage amplifier between room temperature and 165 °C in a Delta 9023 environmental test chamber. $VOSe_2O_5$ was pressed into 12 mm diameter, approximately 1 mm-thick pellets using a cold isostatic press at 3500 psi at room temperature, after which the material was heated to 300 °C for 3 days under dynamic vacuum. Gold was deposited on both sides of the pellet. The unclamped pyroelectric coefficient, defined as dP/dT (change in the polarization with respect to the change in temperature) was determined by measuring the polarization as a function of temperature. A detailed description of the methodology used has been published elsewhere.[36] To determine the ferroelectric behavior, the polarization loop was measured at room temperature under a static electric field of 70 kV/cm at the frequency of 12.5, 16.7, and 20 Hz. For the pyroelectric measurements, the polarization was measured statically from room temperature to 165 °C in 10 °C increments, with an electric field of 60 kV/cm at 100 Hz, 200 Hz, 333 Hz, 500 and 1000 Hz (see Supporting Information, Figure S4). The temperature was allowed to stabilize before the polarization was measured.

Magnetism Measurement. A Quantum Design Magnetic Property Measurement System (MPMS) SQUID magnetometer was used to collect the alternating current (AC) and direct current (DC) magnetic susceptibility on well-ground powder samples since a single crystal of sufficient size and quality could not be obtained. The powders were embedded in paraffin wax within a gelatin capsule to prevent particle motion with the application of large fields. Specific heat data were collected using the semiadiabatic technique as implemented in a Quantum Design Physical Property Measurement System (PPMS). A well ground powder of the title compound was mixed with equal parts by mass of Ag powder and pressed into a pellet to improve thermal coupling. The contribution from Ag was measured separately and subtracted.

Dielectric Measurement. The dielectric properties were measured by attaching polished copper electrodes to opposite faces of a pellet of cold-pressed powder using a fixture built in-house. This fixture was inserted into a Quantum Design PPMS which was used for temperature and field control. An Agilent 4980A LCR meter was used to measure the capacitance which was then converted into the dielectric constant by correcting for the geometry of the sample.

Computational Details

First principles electronic structure calculations were performed using a plane-wave pseudopotential method[37] of density functional theory (DFT)[38,39] as implemented in Quantum ESPRESSO (4.0.1 version) package.[40] Ultrasoft pseudopotentials (USPP)[41] were utilized with a generalized gradient approximation (GGA)[42] for the exchange-correlation corrections. To properly take into consideration the electron correlation in the vanadium 3d states, the GGA plus on-site repulsion U (GGA+U) method[43]

(29) Rodríguez-Carvajal, J. *Phys. B* **1993**, *192*, 55.
(30) Wills, A. S. *Phys. B* **2000**, *276*, 680.
(31) Larson, A. C.; Dreele, R. B. V. *General Structure Analysis System (GSAS)*; Los Alamos National Laboratory Report LAUR; Los Alamos National Laboratory: Los Alamos, NM, 2004; pp 86−748.
(32) Toby, B. H. *J. Appl. Crystallogr.* **2001**, *34*, 210.
(33) Kubelka, P.; Munk, F. Z. *Tech. Phys.* **1931**, *12*, 593.
(34) Tauc, J. *Mater. Res. Bull.* **1970**, *5*, 721.
(35) Kurtz, S. K.; Perry, T. T. *J. Appl. Phys.* **1968**, *39*, 3798.
(36) Ok, K. M.; Chi, E. O.; Halasyamani, P. S. *Chem. Soc. Rev.* **2006**, *35*, 710.
(37) Pickett, W. E. *Comput. Phys. Rep.* **1989**, *9*, 115.
(38) Hohenberg, P.; Kohn, W. *Phys. Rev.* **1964**, *136*, B864.
(39) Kohn, W.; Sham, L. J. *Phys. Rev.* **1965**, *140*, A1133.
(40) Baroni, S.; Corso, A. D.; Gironcoli, S. d.; Giannozzi, P.; Cavazzoni, C.; Ballabio, G.; Scandolo, S.; Chiarotti, G.; Focher, P.; Pasquarello, A.; Laasonen, K.; Trave, A.; Car, R.; Marzari, N.; Kokalj, A., http://www.quantum-espresso.org/.
(41) Vanderbilt, D. *Phys. Rev. B* **1990**, *41*, 7892.
(42) Perdew, J. P.; Burke, K.; Ernzerhof, M. *Phys. Rev. Lett.* **1996**, *77*, 3865.
(43) Anisimov, V. I.; Zaanen, J.; Andersen, O. K. *Phys. Rev. B* **1991**, *44*, 943.

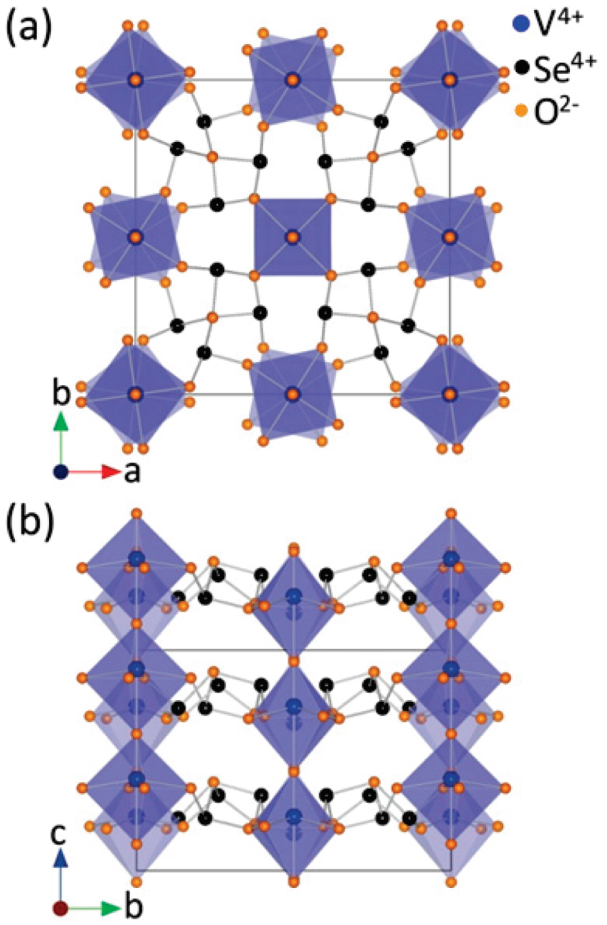

Figure 1. (a) Crystal structure of $VOSe_2O_5$ viewed down the *c*-axis. Note that V(1) and V(2) sit on the 2*a* and 2*b* Wyckoff sites whereas V(3) sits on 4*c*. Such occupancies indicate that the chain composed of V(3) atoms will contain twice as many magnetic sites as the other two chains. (b) View down the *a*-axis so as to emphasize the Se_2O_5 units which join the chains and alternates between running along the *a*- and *b*−axis.

was utilized with different values of effective U (U_{eff}) on the vanadium atoms. To examine the effect of U_{eff} on the relative energies of differently ordered magnetic states, the values of U_{eff} of 1, 2, and 3 eV were employed. A plane wave energy cutoff was set to 37 Ry. A *k*-point grid of 5 × 5 × 9 was used for Brillouin zone integrations. Self-consistency was achieved within the total energy change smaller than 10^{-7} Ry.

Results and Discussion

Recollected Single Crystal Structure. Figure 1 shows the crystal structure of $VOSe_2O_5$ viewed down the *c*- and *a*-axes (space group: *P*4*cc*, $a = 11.2338(8)$ Å, $c = 7.8711(11)$ Å, $Z = 8$). The linear chains of corner-shared VO_6 octahedra run parallel to the *c*-direction. There are three crystallographically unique vanadium cations that we will refer to as V(1), V(2), and V(3). The unique cations are found on the corners, body-center, and edges of the unit cell, respectively. The V(1)- and V(3)-chains are gauche-type with alternating rotations of ±16.4(1)° and ±24.3(1)° of the adjacent octahedra, respectively, down the length of the chains, whereas the V(2)-chain is eclipse-type, that is, the octahedra do not rotate down the length of the chain. Figure 2 shows three individual VO_6 chains where the V^{4+} cations are shifted along the *c*-direction by an amount Δd_z from their octahedral centers. The values of Δd_z are +0.322, +0.391, and −0.328 Å for the V(1), V(2), and V(3) cations, respectively. Thus, for each V^{4+} cation, there are four equivalent V−O equatorial bonds as well as one short and one long axial bond. The short and long bonds are in the range of 1.593(3) Å to 1.630(6) Å and 2.305(6) Å to 2.341(3) Å, respectively. The equatorial V−O bonds range between 1.973(2) Å to 2.002(2) Å. The chains are connected by two SeO_3 trigonal pyramids that share corners to form a Se_2O_5 group. The stereochemically active lone-pairs on the Se^{4+} cation are pointed in antiparallel directions. The Se−O bonds range between 1.647(3) Å to 1.823(2) Å. Bond valence sum calculations[44,45] resulted in values near 3.9 for the Se^{4+} cations and between 4.1 and 4.2 for the V^{4+} cations.

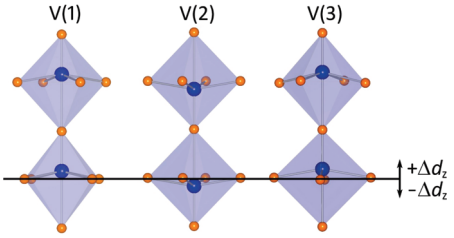

Figure 2. Individual V(1), V(2), and V(3) chains. The black solid line represents the equatorial planes and is drawn to guide the eye. The Δd_z indicates the displacements of V^{4+} ions from the octahedral centers along the *c*-direction.

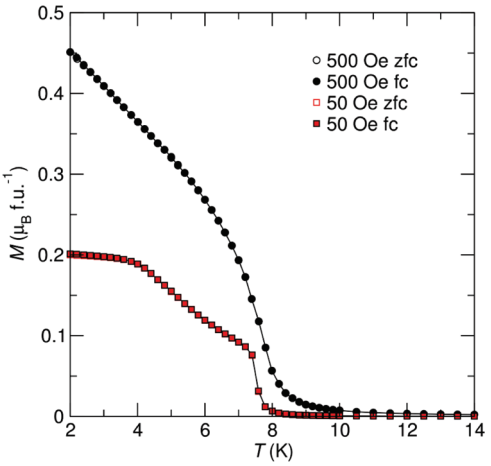

Figure 3. Temperature-dependent magnetization of $VOSe_2O_5$ collected under magnetic fields of 50 and 500 Oe. Empty and filled circles present zero-field cooled (ZFC) and field cooled (FC) DC magnetic susceptibilities, respectively. Note that there is no deviation between the ZFC and FC data. The magnetic ordering temperature is found to be 8 K with subsequent changes to the slope of the curves around 7 and 4 K.

DC and AC Magnetization and Heat Capacity Measurements. The temperature dependence of the DC magnetic susceptibility was measured under field cooled (FC) and zero field cooled (ZFC) conditions at both 50 and 500 Oe (see Figure 3). A transition to a magnetically ordered phase is found near 8 K. Interestingly, there is a change in the slope at 4 and 7 K in the susceptibility measured at 50 Oe that is not observed for data measured at 500 Oe.

(44) Brese, N. E.; Okeeffe, M. *Acta Crystallogr., Sect. B* **1991**, *47*, 192.
(45) Brown, I. D.; Altermatt, D. *Acta Crystallogr.* **1985**, *B41*, 244.

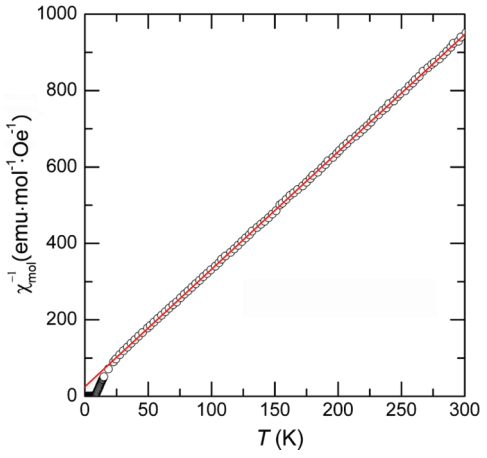

Figure 4. Inverse magnetic susceptibility of $VOSe_2O_5$ collected under a 1000 Oe field and the fit of the susceptibility data (25−300K) to the Curie−Weiss equation.

Additionally, the change near 4 K is not observed when measured in the presence of the larger magnetic fields.

As seen in Figure 4, the inverse magnetic susceptibility data from 25 to 300 K fits well to a modified Curie−Weiss equation given as $C/(T - \Theta_{CW}) + \chi_0$ where C, Θ_{CW}, and χ_0 represent the Curie constant, the Weiss temperature, and a temperature independent term, respectively. From the Curie constant an effective moment, μ_{eff}, of 1.69 μ_B was obtained. The value agrees well with the theoretical spin-only value of 1.73 μ_B for V^{4+}. A Weiss temperature, Θ_{CW}, of −8.9 K was determined, that indicates the dominant interaction is most likely antiferromagnetic coupling between spins. The temperature independent term was estimated to be -3.2×10^{-4} emu mol^{-1} Oe^{-1} and likely reflects the diamagnetic contribution from the straw, gel cap, and wax that held the sample during the measurement.

Isothermal magnetization traces at different temperatures above and below the ordering temperature of 8 K were also measured (see Figure 5a). Below 8 K the magnetization rapidly increases and exhibits the hysteretic behavior of a soft ferromagnet with a coercive field on the order of tens of Oe (see Figure 5b). However, the trace taken at 2 K saturates to a value of 4 μ_B per unit cell that corresponds to a value of 0.5 μ_B per formula unit (f.u.$^{-1}$) with the application of a few hundred Oe. Unexpectedly, this saturated magnetic moment of 0.5 μ_Bf.u.$^{-1}$ is one-half the value for a fully saturated ferromagnetic alignment of V^{4+} (d^1, $\mathbf{S} = 1/2$, $\mathbf{L} = 2$). To accurately obtain the Curie temperature, the magnetization curves were plotted in the style of Arrot (M^3 vs H) as shown in Figure 5c where the linear behavior of the 8 K data reflects that this is very near the long-range ordering temperature.[46]

The real part of the AC magnetic susceptibility, collected in the absence of an external DC field, indicates the behavior of the low-field DC susceptibility curves with no frequency dependence observed for frequencies of 1 Hz, 10 Hz, 100 Hz or 1000 Hz (see Figure 6a). The imaginary part of the susceptibility, however, does exhibit anomalies that correlate to the changes in the slope of the low field

(46) Arrott, A. *Phys. Rev.* **1957**, *108*, 1394.

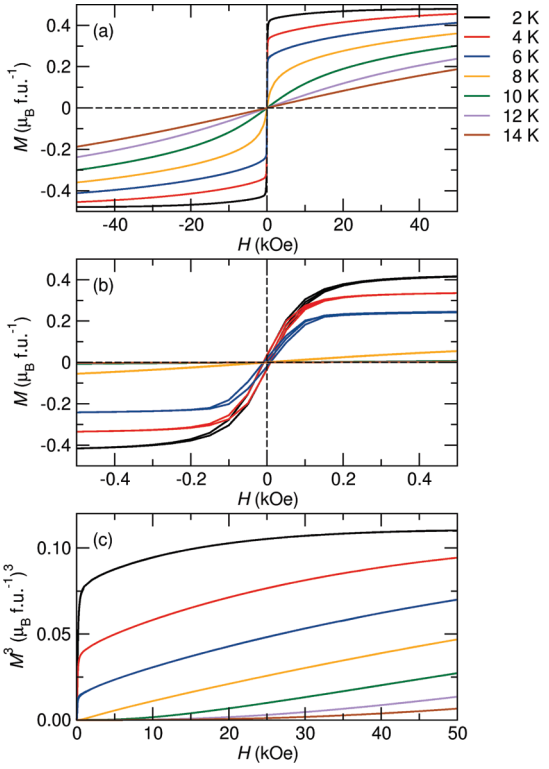

Figure 5. (a) Isothermal magnetization curves of $VOSe_2O_5$ measured at different temperatures above and below the magnetic ordering transition. (b) Magnetization curves expanded around the origin to show the small coercive field. (c) Magnetization curves plotted in the style of Arrott to emphasize the true Curie temperature as indicated by the approximately straight line at 8 K.

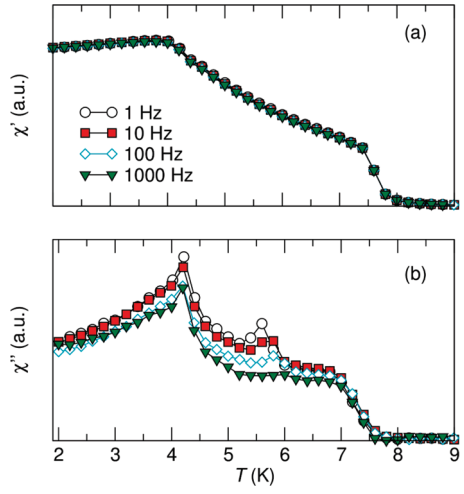

Figure 6. (a) Real and (b) imaginary part of the AC magnetic susceptibility collected at frequencies of 1, 10, 100, and 1000 Hz. Note that the peak at 5.5 K has strong frequency dependence and is suppressed in the presence of very high frequency fields in the imaginary component.

susceptibility data. Three peaks are observed in the imaginary part of the AC susceptibility that could reflect the possibility of three different magnetic transitions. Additionally, the 5.5 K peak reveals a frequency dependence that may indicate some short-range fluctuations which may be associated with relatively delocalized magnetic interaction pathways through the nearest neighbor (NN) *interchain* magnetic interactions in the *ab*-plane (see below).

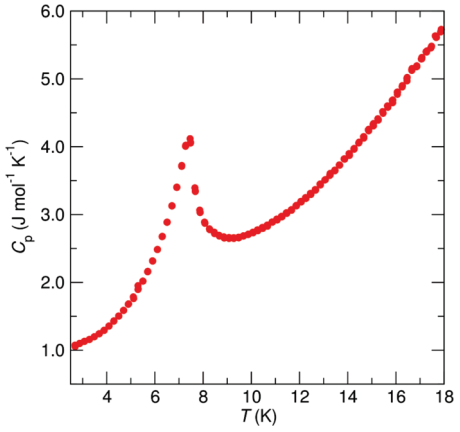

Figure 7. Specific heat of $VOSe_2O_5$ as a function of temperature measured upon cooling. Note the λ-anomaly that has a peak occurring at ~7 K signaling the onset of long-range magnetic ordering.

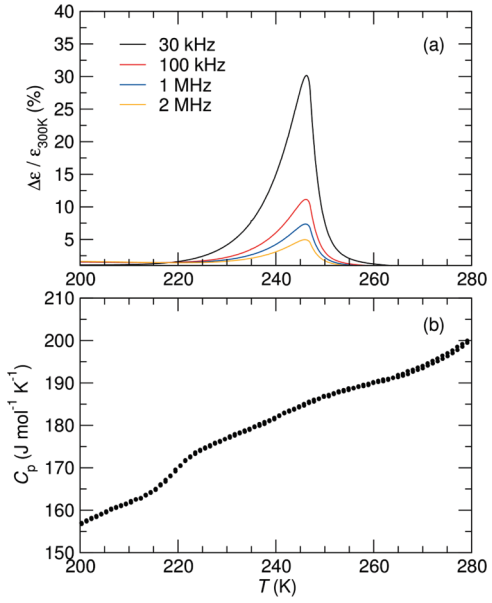

Figure 8. (a) Temperature dependence of the dielectric constant for $VOSe_2O_5$ for different frequencies normalized to the room temperature value. Note the anomaly observed near 240 K. (b) High temperature region of the specific heat. The broad hump observed from 220 to 260 K corresponds well to the anomaly in the dielectric data.

In addition to the magnetic measurements, the specific heat of $VOSe_2O_5$ was also investigated. The specific heat of $VOSe_2O_5$ was measured between 2.5 and 300 K. Near the magnetic ordering temperature (see Figure 7), a single λ-type anomaly is observed near 7 K that indicates the rise of three-dimensional long-range magnetic ordering. Finally, the temperature dependence of the dielectric constant was investigated (see Figure 8a). At low temperatures, no evidence of an anomaly near the magnetic ordering temperature was observed. However, a broad peak that corresponded to a 30% increase in the dielectric constant was found to occur around 240 K. Similarly, the high temperature region of the heat capacity also reflects some additional features occurring in this temperature region (see Figure 8b). No change in the feature was found with the application of a magnetic field, and no changes to the crystal structure were found in the neutron

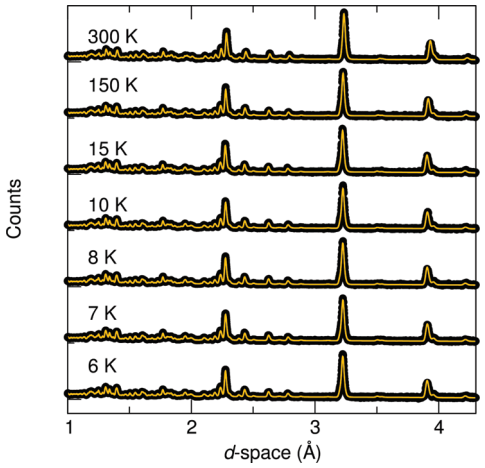

Figure 9. Refinement of the TOF neutron diffraction data at different temperatures. No extra peaks are observed below the magnetic ordering temperature indicating that the magnetic structure must be fully contained within the room temperature description of the structure.

Table 4. Relative Energies ΔE (meV per unit cell) of Different Magnetic States of $VOSe_2O_5$ Obtained from GGA+U (U_{eff} = 1, 2, and 3 eV) Calculations

	ΔE (meV)		
magnetic state	U_{eff} = 1 eV	U_{eff} = 2 eV	U_{eff} = 3 eV
AF2 (4 μ_B)	4.4	4.1	3.8
AF6 (6 μ_B)	1.2	1.5	1.7
AF4 (0 μ_B)	−0.6	0	0.7
FM (8 μ_B)	0	0	0
AF7 (4 μ_B)	−14	−11	−6.6
AF5 (6 μ_B)	−16	−12	−8.8
AF3 (0 μ_B)	−28	−20	−15
[a]AF1(4 μ_B)	−33	−24	−18

[a] The calculated ground state.

diffraction data in this temperature range. An electronic effect is also negligible from our preliminary electrical resistivity measurement. At present the origin of the dielectric anomaly is unclear.

Magnetic Structure Determination. Figure 9 shows the neutron powder diffraction (NPD) patterns of $VOSe_2O_5$ collected at 6, 7, 8, 10, 15, 150, and 300 K in time-of-flight mode at Los Alamos National Laboratory. There is no indication of a structural phase transition at any of the measured temperatures (see Figure 9), and a summary of the results of the structural refinements is included in Table 5. Nor is there any evidence of new magnetic reflections below the ordering temperature of 8 K. This means that a spin structure which develops below the ordering temperature has the same unit cell of the crystal structure. It is important to note that the multiplicity of the V^{4+} cations is not equivalent. V(1) and V(2) occupy the 2*a* and 2*b* Wyckoff positions whereas V(3) occupies 4*c*. Thus several plausible spin alignments with 4 μ_B per unit cell were adopted for the refinements of the neutron diffraction data. For example, each chain has its spins ferromagnetically aligned, whereas the spins are antiferromagnetically arranged between the V(1)- and V(2)-chains and between the V(2)- and V(3)-chains. However, the additional intensities attributable to magnetic contributions

Table 5. Summary of Results from the Rietveld Structure Refinement to the Nuclear Part of the Variable Temperature TOF Neutron Diffraction Patterns[a]

	300 K	150 K	15 K	10 K	8 K	7 K	6 K
a (Å)	11.2263(2)	11.1999(6)	11.1977(3)	11.1957(1)	11.1932(1)	11.1931(3)	11.1948(2)
c (Å)	7.8689(2)	7.8306(2)	7.8170(2)	7.8161(2)	7.8141(2)	7.8134(2)	7.8148(2)
V (Å^3)	991.73(4)	982.42(9)	980.25(7)	979.71(2)	979.01(2)	978.92(7)	979.38(5)
R_p (%)	2.30	2.27	2.23	2.28	2.05	2.09	2.08
R_{wp} (%)	3.30	3.31	3.38	3.31	3.03	3.08	3.05
χ^2	1.984	1.294	1.305	1.344	1.292	1.264	1.245

[a] R_p and R_{wp} are given for the highest resolution bank of detectors.

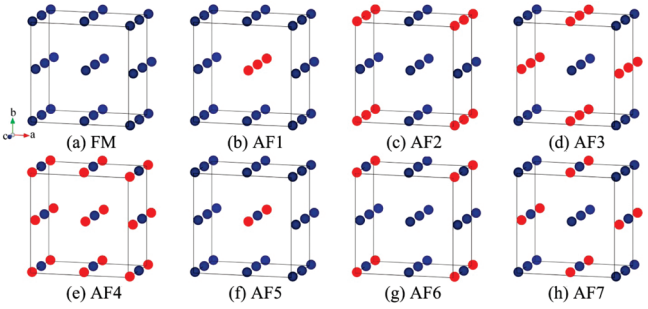

Figure 10. Schematic representations of the eight different spin states employed to evaluate magnetic exchange parameters, J. For clarity, only the V sites are present with blue-filled circle (up-spin) and red-filled circle (down-spin).

in the data taken below 8 K were too weak to complete the refinements of spin alignments, and DFT calculations with a variety of ordered magnetic states were performed to ascertain the magnetic ground state. We considered a total of eight different magnetic states calculated using the GGA+U method (U_{eff} set at 1, 2, and 3 eV). We note that the GGA+U method would not be appropriate if $VOSe_2O_5$ exhibited any orbital degeneracy. However, the highly distorted VO_6 octahedra in the structure ensure that this is not the case. Spin polarized state calculations with GGA alone result in metallic states for $VOSe_2O_5$. One ferromagnetic (FM) and seven antiferromagnetic orderings (AF1−AF7) of the spin of V^{4+} cations are shown in Figure 10 where the unit cell of their magnetic structures is equivalent to that of the crystal structure. Their relative energies with the different U_{eff} values are listed in Table 4 where the ferromagnetic state energy was set to zero.

Our calculations indicate that the FM state cannot be the ground state, since all values of U_{eff} result in four different antiferromagentic states (AF1, AF3, AF5, AF7 states) which have lower total energies. The order of the magnetic states in energy is retained with respect to the U_{eff} values except for the AF4 state that is almost degenerate with the FM state. The calculated ground state is the AF1 state in which the spins in each intrachain are ferromagnetically aligned whereas the spins between the V(1)−V(2) and V(2)−V(3) interchains are antiferromagnetically arranged. The AF1 state has 4 μ_B per unit cell that is consistent with our isothermal magnetization data. As shown in Figure 11, the total and projected densities of states (DOS) for the AF1 state with $U_{eff} = 2$ eV show an energy band gap at the Fermi level that is also in agreement with the insulating nature of the title compound.

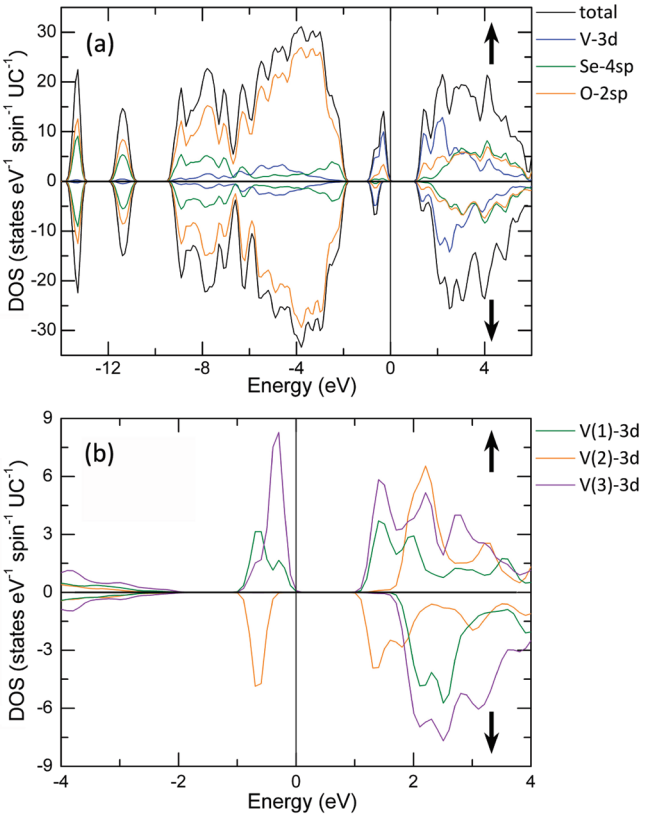

Figure 11. Total density of states (TDOS) and projected DOSs (PDOSs) of V-3d, Se-4sp, and O-2sp of the AF1 state calculated with GGA+U (U_{eff} = 2 eV). PDOSs plots for the 3d orbitals of V(1), V(2), and V(3).

The projected DOSs (PDOSs) of the V-3d exhibit oppositely spin polarized 3d states, that is, the V(1) and V(3) are positively spin polarized whereas the V(2) is negatively spin polarized. On the basis of the DFT calculations, the proposed AF1 magnetic structure was refined against the low temperature neutron data (see Figure 12).

The details of the basis vectors associated with the allowed orientation of the spins are listed in Supporting Information, Tables S2 and S3. The symmetry of the crystal allows the spins to point along the a-, b-, or c-axis and all orientations were considered with the lowest R_{mag} (15%) corresponding to the spins forming a tilted antiferromagnetic structure similar to AF1 with the spins laying in the ab-plane. The best refinements were obtained from ferromagnetic (FM) or antiferromagnetic (AF4) alignments, as well as a commensurate spin density wave (SDW) (see Supporting Information, Figure S5) that were identified based upon symmetry analysis. With the FM and AF4 alignments, the spins are parallel to the

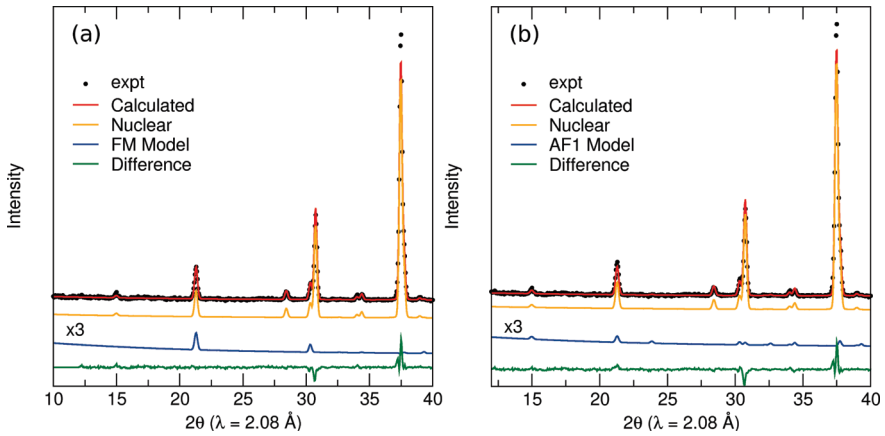

Figure 12. Low angle region of the constant wavelength neutron data collected at BT-1 at 6 K. Note that while the ferromagnetic fit shown in (a) corresponds to the best model refined, in reality the contribution from magnetic reflections is so small that obtaining a good fit is very difficult. Particularly notice that the magnetic intensity on the peak at 15° and 35° is completely missed by the ferromagnetic model whereas the model corresponding to AF1 shown in (b) does capture these features.

c-axis. For the three magnetic states, FM, AF4, and SDW, the reliability factors from the refinements were nearly equal, $R_{mag} \sim 5.6\%$ (see Supporting Information, Table S1). However, these three magnetic states contradict the magnetic susceptibility and magnetization data. The actual magnetic information from the neutron diffraction data is very limited attributable to the small effective ordered moment on vanadium. Therefore the calculated AF1 state appears to be the most reasonable state, consistent with the magnetic and specific heat data.

To further evaluate the magnetic interactions, we attempted to extract magnetic exchange parameters (J) by assuming pairwise magnetic interactions with the calculated energy of the eight magnetic states.[47,48] Three different V^{4+} *intrachain* interactions (J_1, J_2, and J_3,) and four different V^{4+} *interchain* interactions (J_{12}, J_{13}, J_{23}, and J_{33}) were considered. To evaluate the magnetic exchange parameters, we performed mapping analysis based on our DFT calculations. Since we have the relative energies of the eight ordered magnetic states (see Table 4), we can express a magnetic exchange parameter with differently combined magnetic states. The energies of the eight ordered magnetic states can be written in terms of spin Hamiltonian,

$$H = -\sum_{i<j} J_{ij}\hat{S}_i \cdot \hat{S}_j$$

where J_{ij} ($= J_1, J_2, J_3, J_{12}, J_{13}, J_{23}$, and J_{33}) is the magnetic exchange parameter for the pairwise magnetic interaction between the magnetic sites i and j, and $\hat{S}_i$ and $\hat{S}_j$ are the spin angular momentum operators at the magnetic sites i and j, respectively. The total magnetic exchange energy of the eight magnetic states can be described as

$$E_{FM} = \frac{N^2}{4}(-8J_{13} - 8J_{23} - 8J_{12} - 8J_{33} - 2J_1 - 2J_2 - 4J_3)$$

$$E_{AF1} = \frac{N^2}{4}(8J_{13} - 8J_{23} + 8J_{12} - 8J_{33} - 2J_1 - 2J_2 - 4J_3)$$

$$E_{AF2} = \frac{N^2}{4}(8J_{13} + 8J_{23} - 8J_{12} - 8J_{33} - 2J_1 - 2J_2 - 4J_3)$$

$$E_{AF3} = \frac{N^2}{4}(-8J_{13} + 8J_{23} + 8J_{12} - 8J_{33} - 2J_1 - 2J_2 - 4J_3)$$

$$E_{AF4} = \frac{N^2}{4}(-8J_{13} - 8J_{23} - 8J_{12} - 8J_{33} + 2J_1 + 2J_2 + 4J_3)$$

$$E_{AF5} = \frac{N^2}{4}(-8J_{23} - 8J_{33} + 2J_1 - 2J_2 - 4J_3)$$

$$E_{AF6} = \frac{N^2}{4}(8J_{13} - 8J_{12} - 8J_{33} - 2J_1 - 2J_2 + 4J_3)$$

$$E_{AF7} = \frac{N^2}{4}(-8J_{13} - 8J_{33} - 2J_1 + 2J_2 - 4J_3)$$

where N defined as unpaired electrons per magnetic site is 1.[47,48] Our calculations revealed that the J values were, unexpectedly, inconsistent, that is, different expressions for the same parameter gave different values. This inconsistency may be indicative of the magnetic exchange interactions that are not well localized despite the insulating nature of $VOSe_2O_5$. As seen in Figure 13, there are four different *interchain* magnetic interaction pathways. Two may be considered nearest neighbor (NN) interactions, that is, between the V(1) and the V(3) cations and between the V(2) and the V(3) cations, J_{13} and J_{23}, respectively, and two are next nearest neighbor (NNN) interactions, that is, between the V(1) and V(2) cations and two symmetry equivalent V(3) cations, J_{12} and J_{33}, respectively. With the NN interactions, two pathways are possible, a "short" pathway, for example, V(1) − O − Se − O − V(3), and a "long" pathway, for example, V(1) − O − Se − O − Se − O − V(3). For the NNN interactions, only a "long" pathway is possible, for example, V(1) − O − Se − O − Se − O − V(2), that is nearly equivalent to the long NN pathway (see Figure 13). Clearly the strongest magnetic interactions would be through the short NN pathway. We suggest, however, that the long NN and NNN magnetic interactions are not negligible, and manifest themselves

(47) Dai, D.; Whangbo, M.-H. *J. Chem. Phys.* **2001**, *114*, 28873.
(48) Dai, D.; Whangbo, M.-H. *J. Chem. Phys.* **2003**, *118*, 29.

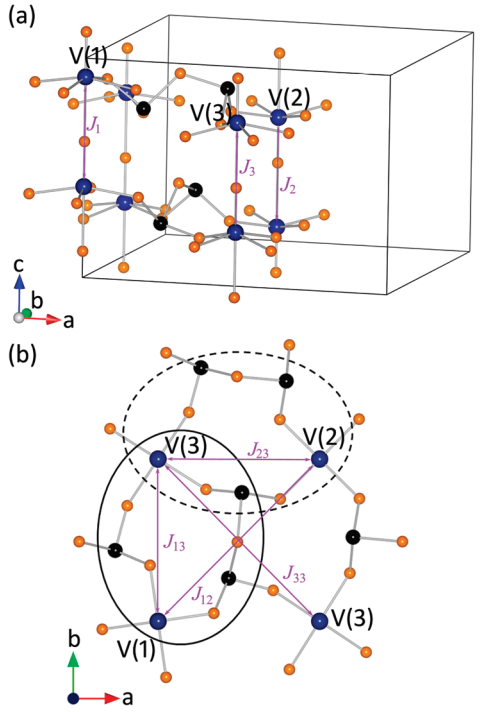

Figure 13. (a) Three *intrachain* magnetic interactions given as J_1, J_2, and J_3 are exhibited. (b) Four *interchain* magnetic interactions given as J_{13}, J_{23}, J_{12}, and J_{33} are shown. J_{13} and J_{23} represent nearest neighbor (NN) interactions, whereas J_{12} and J_{33} represent next nearest neighbor (NNN) interactions. Note that with the NN interactions, "short" and "long" pathways are possible, for example, V(1) − O − Se − O − V(3) and V(1) − O − Se − O − Se − O − V(2), respectively. Two possible magnetic exchange pathways of the magnetic interactions are enclosed in the black solid and dashed ellipses, respectively.

through the observed frequency dependence in the AC magnetic susceptibility. There is support for our interpretation if we examine the magnetic behavior of other V^{4+} oxides, specifically Li_2VOTO_4 (T = Si^{4+} or Ge^{4+})[49] and $VOMoO_4$.[50] These oxides were shown to be two-dimensional spin-half antiferromagnets, where the NN and NNN interactions are mediated by non-magnetic polyhedra, that is, TO_4 or MoO_4 tetrahedra. In fact, it is theoretically predicted that the relative strength of the NNN/NN ratio could give rise to spin fluctuations in the spin-half frustrated square lattice.[51,52] Thus, the observed frequency dependence in the AC magnetic susceptibility may reflect this feature of the spin frustration.

Non-Centrosymmetric Functional Properties. $VOSe_2O_5$ is non-centrosymmetric and polar; that encouraged us to investigate its second-harmonic generation (SHG) and polarization properties. Powder SHG measurements[35,36] using 1064 nm radiation indicated $VOSe_2O_5$ has a SHG efficiency comparable to α-SiO_2. The relatively weak SHG efficiency may be understood by closely examining the structure. There are two acentric polyhedra that can contribute to the SHG, the SeO_3 trigonal pyramids and the VO_6 octahedra. Although the Se^{4+} cation is in a highly asymmetric coordination environment, the net polarization attributable to the SeO_3 groups is minimal. The polarization associated with the SeO_3 trigonal pyramids are directed in an antiparallel manner with respect to neighboring units, canceling any contribution to the SHG efficiency. With the V^{4+} cations, there is a *net* polarization along the *c*-axis, as a result of unequal cancelation of the V^{4+} moments. Thus, the SHG contribution from the VO_6 octahedra is reduced. Finally, $VOSe_2O_5$ is green indicating some of the frequency doubled radiation from a 1064 nm source will be absorbed. All of these factors result in a weak SHG efficiency and negligible size dependence. The polarization of $VOSe_2O_5$ was measured from room temperature to 210 °C. The measurements clearly indicated that although $VOSe_2O_5$ is polar, the material is not ferroelectric, that is, the polarization is not reversible in the presence of an external electric field. The observed "ferroelectric-like" polarization loops are attributable to dielectric loss and not polarization reversal. These polarization measurements indicate that the macroscopic polarization in $VOSe_2O_5$ cannot be reversed in the presence of an external electric field. The experimental results are consistent with our frozen phonon DFT calculation results with the AF1 state at U_{eff} = 2 eV. It is reasonable to assume that the electric polarization in $VOSe_2O_5$ is mainly attributable to the off-centered V^{4+} cations, since the polarization associated with the SeO_3 groups are pointed in antiparallel directions. It is also known that an umbrella-type inversion of SeO_3 is energetically unfavorable and therefore not likely to occur.[53] Subsequently, the only manner in which electrical polarization reversal may occur is via the displacement of V^{4+} cation parallel to the *c*-axis in each VO_6 chain. Our calculations in the AF1 with U_{eff} = 2 eV indicate that for the inversion process, $\sim 6.0 \times 10^{-1}$ eV per VO_6 is required on average. This energy is higher than those calculated in well-known ferroelectrics such as $BaTiO_3$ ($\sim 1.8 \times 10^{-2}$ eV) and $PbTiO_3$ ($\sim 2.0 \times 10^{-1}$ eV).[54] $VOSe_2O_5$ is, however, pyroelectric: the macroscopic polarization changes as a function of temperature. The pyroelectric constant of $VOSe_2O_5$ given as the first derivative of spontaneous polarization with respect to temperature is of $\sim -20\ \mu C/m^2 \cdot K$ at 75 °C.

Conclusion

Through our investigation of the magnetic, dielectric, and functional properties of $VOSe_2O_5$, we demonstrated that the material undergoes three magnetic transitions near 4, 5.5, and 8 K. The long-range magnetic ordering occurs at 8 K, and the magnetic behavior is ferrimagnetic below 8 K. The ferrimagnetic behavior is consistent with our neutron diffraction data as well as our DFT calculations. The frequency dependence of the AC magnetic susceptibility observed near 5.5 K may be associated with

(49) Rosner, H.; Singh, R. R. P.; Zheng, W. H.; Oitmaa, J.; Drechsler, S. L.; Pickett, W. E. *Phys. Rev. Lett.* **2002**, *88*, 186405–1.
(50) Bombardi, A.; Chapon, L. C.; Margiolaki, I.; Mazzoli, C.; Gonthier, S.; Duc, F.; Radaelli, P. G. *Phys. Rev. B* **2005**, *71*, 220406.
(51) Nath, R.; Tsirlin, A. A.; Rosner, H.; Geibel, C. *Phys. Rev. B* **2008**, *78*, 064422-1.
(52) Schmidt, B.; Thalmeier, P.; Shannon, N. *Phys. Rev. B* **2007**, *76*, 125113.
(53) Kim, S.-H.; Yeon, J.; Halasyamani, P. S. *Chem. Mater.* **2009**, *21*, 5335.
(54) Cohen, R. E. *Nature* **1992**, *358*, 136.

NN and NNN *interchain* magnetic interactions. This is also compatible with the inconsistent magnetic exchange parameters extracted from our DFT calculations, attributable to the magnetic interaction pathways being not well localized. Finally, although $VOSe_2O_5$ is ferrimagnetic and polar, the material is not multiferroic since the macroscopic polarization is not switchable, that is, $VOSe_2O_5$ is not ferroelectric, attributable to the energetically unfavorable VO_6 polarization inversion. The concurrent observation of SHG intensity in a magnetically ordered material suggests possible exotic non-linear magneto-optical behavior in this material. The dielectric anomaly near 240 K also bears further investigation.

Acknowledgment. S.-H.K. and P.S.H. thank the Welch Foundation (Grant E-1457), NSF (DMR-0652150), and ACS PRF (47345-AC10) for support. B.C.M. and R.S acknowledge the National Science Foundation for support through Career Awards to R.S. (DMR 0449354) and for the use of MRSEC facilities at UCSB (DMR 0520415). D.P. Shoemaker and A. Llobet are thanked for their assistance in data collection at Los Alamos National Lab. Research is also sponsored by the Division of Materials Science and Engineering, Office of Basic Energy Sciences. Oak Ridge National Laboratory is managed by UT-Battelle, LLC, for the U.S. Department of Energy under Contract DE-AC05-00OR22725. We acknowledge the support of the National Institute of Standards and Technology, U.S. Department of Commerce, in providing the neutron research facilities used in this work. Certain commercial equipment, instruments, or materials are identified in this paper to foster understanding. Such identification does not imply recommendation or endorsement by the National Institute of Standards and Technology, nor does it imply that the materials or equipment identified are necessarily the best available for the purpose.

Supporting Information Available: Additional experimental data. This material is available free of charge via the Internet at http://pubs.acs.org.